Digital 3D Animation of Powder-Snow Avalanches

Filipe Nascimento[§]
ICMC-USP, Brazil

Afonso Paiva
ICMC-USP, Brazil

Abstract—Physically based animation of fluids such as smoke, water, and fire provides some of the most stunning computer graphics in the entertainment industry. However, several phenomena still need to be fully understood, and their formulations are still the focus of intense research in other fields, such as Physics and Civil Engineering. That is the case with snow avalanches, whose numerical modeling is challenging due to their complex dynamics. The manipulation of such phenomena is new to computer graphics, and few works exist. This project aims to bring these formulations to the field of computer graphics regarding the digital animation of powder-snow avalanches.

I. Introduction

Avalanches arise from an instability in the accumulated snow cover on a mountain surface. Beyond the slope of the terrain, other factors can influence the release process: the roughness of the terrain, the structure of the snow cover, and weather conditions [1]. Snow avalanches can be classified according to their motion [2]:

- **Flowing avalanche** has a high-density core consisting of snow and heavy ice, leading to a gravity-driven laminar flow, where the mountain topography shapes its trajectory. This dense snow layer accelerates quickly, increasing in mass and volume as more snow becomes entrained;
- **Powder-snow avalanche** A Powder-snow avalanche begins with a flowing snow avalanche that causes snow particles to mix with the air due to turbulent motion, forming a suspended cloud of powder-snow, i.e., a particle-laden *gravity current* [3].

We introduce a numerical framework based on the Finite Volume Method to simulate the dynamics of a powder-snow avalanche under complex terrains. Our framework separates the avalanche into two main layers: dense and powder-snow layers. The flow of the dense snow layer is simulated by solving a type of Shallow Water Equations suited for complex terrains, known as *Savage-Hutter model*. The powder-snow layer flow is modeled as a miscible mixture of two fluids and simulated using the incompressible Navier-Stokes equations. Additionally, the method couples both layers by transferring mass and momentum toward the powder-snow layer. Fig. 1 shows our method in action.

A. Contributions

In summary, our key contributions are:

- We present a comprehensive two-layer framework for physically-based simulation of powder-snow avalanches,

Fig. 1: A large-scale simulation of a powder-snow avalanche using the Finite Volume Method in a mesh with 17.8M cells and a total volume of $0.43km^3$. A turbulent powder-snow cloud forms as the avalanche travels a distance of $1.5km$. The plume billow structures arise due to a novel procedural snow entrainment process modeled by our method.

which includes the interaction of the dense-snow avalanche with the terrain and the turbulent motion of the powder-snow cloud in suspension (Section IV);

- A transition layer model based on a novel procedural snow entrainment mechanism that enables the coupling between the dense-snow layer and the powder-snow layer, allowing the transference of mass and momentum to the powder-snow layer (Sections III-C and IV-A);
- Since the frontal region of the avalanche feeds an energetic turbulent powder-snow cloud, we introduce a fast algorithm for computing the avalanche front distance field, which impacts the formation of the plume structures (Section V-A).
- We present an accurate partition of unity interpolation scheme for mesh data conversion to render the powder-snow clouds on large terrains. (Section V-B).

In the related thesis, extensive research on avalanche is presented and a recent survey can be found in [4].

II. Powder-Snow Avalanche in a Nutshell

In literature, a powder snow-avalanche (PSA), a.k.a. *mixed-motion avalanche*, usually consists of two main layers [5], [6]: the *dense-snow layer* (DSL) and the *powder-snow layer* (PSL), representing the flowing avalanche and the powder avalanche, respectively. In addition, two extra layers are used to explain the changes in mass observed in the DSL and PSL. The first layer, referred to here as the *ground layer*, consists of the snow

cover available in the terrain. The second layer, referred to as the *transition layer* (TL), appears between the DSL and the PSL. This layer is responsible for the exchange of mass and momentum between the two main layers. Table I lists the four mentioned layers and their main characteristics.

TABLE I: Layers of a powder-snow avalanche.

layer	description	flow type
PSL	suspension layer	turbulent particle-laden flow
TL	two-phase viscous wall layer	two-phase flow
DSL	flowing avalanche layer	laminar flow
Ground	stagnant snow layer	snow at rest

During a PSA, the DSL may gain mass from the ground layer by snow entrainment and lose mass from snow deposition processes. However, there are also exchanges between the DSL and the PSL. As collisions fracture large chunks of snow, the DSL surface becomes fluidized. The increasing wind causes particles to leave the DSL surface in ballistic motion, creating a transition region. Some particles go up to the PSL, where collisions are less frequent and get into strong aerodynamic turbulence. Figure 2 depicts the PSA anatomy.
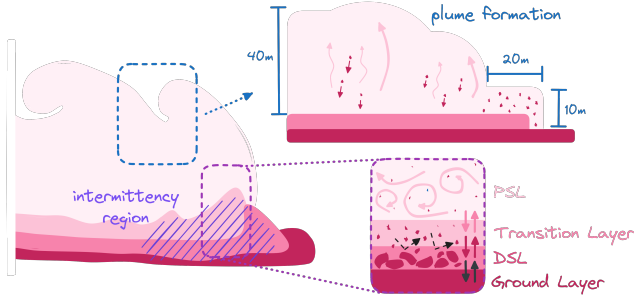

Fig. 2: The different layers that compose a PSA. In the leading edge, snow can be plowed frontwards but can also be violently ejected into the air by eruption. Plumes are born from the snow eruption, growing as heavy particles settle down and displace air upwards. The intermittency region includes surges of rapid flows and produces the oscillatory behavior of the PSA front.

The snow entrainment plays a central role in the evolution of an avalanche flow, particularly in a PSA. The entrainment process feeds the PSL, dictating the powder-snow cloud's size. There are some fundamental mechanisms of entrainment in snow avalanches [7]–[9]: frontal *plowing*, *eruption*, and *basal erosion*. Figure 2 shows the snow entrainment mechanisms in PSAs.

The plowing and eruption mechanisms are essential for forming plume structures in a powder-snow cloud. Some researchers [10] observed that after an initial plume quickly achieves $10m$ of height, the growth pauses and resumes as the plume is no longer at the avalanche front (at least $20m$ behind). Another ingredient for the *plume formation* is the oscillatory behavior in the *intermittency region* [11].

III. GOVERNING EQUATIONS

Here, we briefly present the governing equations and theoretical background for modeling a PSA. As described in

TABLE II: Notations used in DSL and PSL models.

layer	notation	meaning	unit
both	t	time	s
	$\mathbf{x}$	position	m
	$\mathbf{g}$	gravitational acceleration	$kg/m.s^2$
DSL	$\bar{\mathbf{u}}$	depth-averaged flow velocity	m/s
	$\bar{p}$	basal pressure	$kg/m.s^2$
	h	avalanche flow height	m
	h_s	snow cover thickness	m
	$\bar{\rho}_s$	snow density	kg/m^3
	q_{er}	snow entrainment rate	$kg/m.s^2$
	$\boldsymbol{\tau}_b$	basal shear stress	$kg/m.s^2$
	υ	Voellmy dry friction	$-$
	ξ	Voellmy dynamic friction	m/s^2
	E_b	specific erosion energy	m^2/s^2
PSL	$\hat{\mathbf{u}}$	air-snow mixture velocity	m/s
	$\hat{p}$	air-snow mixture pressure	$kg/m.s^2$
	ρ	air-snow mixture density	kg/m^3
	$\hat{\rho}_k$	reference density of phase k	kg/m^3
	μ	air-snow mixture viscosity	$kg/m.s$
	$\hat{\mu}_k$	reference viscosity of phase k	$kg/m.s$
	α	powder-snow volume fraction	$-$
	α_a	ambient air volume fraction	$-$
	Γ	diffusion coefficient	m^2/s

Section II, a PSA consists of four main layers: a ground layer representing the snow cover encountered in the mountain, the DSL, the TL, and the PSL. In order to guide our choices, we make the following assumptions:

> **A1.** *The layers' physical characteristics are sufficiently different to justify different governing equations to explain their respective flow regime.*
> **A2.** *The TL is considered a rough wall that coincides with the surface avalanche of the DSL. The wall moves at the same speed as the DSL.*
> **A3.** *Neither the turbulent air nor the deposition processes of the PSL are significant enough to have any effect on the motion or mass of the DSL. Therefore, the influence of the PSL in the DSL is negligible.*

The DSL and PSL models are described by PDEs derived from physical laws of conservation of mass and momentum. Table II lists physical quantities involved in the models. Next, we will describe the governing equations of each main layer.

A. Dense-Snow Layer Model

This section describes the mechanical model for simulating the dense flow avalanche corresponding to the DSL. The key idea is to consider that the DSL behaves as a granular material that undergoes high deformation, driven by basal friction against the gravitational force in inclined terrain.

Our approach resorts to an improved SWE-based model to describe the granular flow, the Savage-Hutter (SH) model [12]. The SH extends the SWE by introducing a Coulomb-like basal friction and a yield criterion to handle the internal friction. Additionally, the SH tackles the inherent limitation of the SWE for steep slopes by describing its equations with a local curvilinear coordinate system.

In order to employ a curvature-free description for complex reliefs and to avoid complicated governing equations induced by curvilinear coordinate transformations, we adopt a *surface*

PDE (SPDE) version of SH equations [13], [14]. Let $\mathcal{S}_b \subset \mathbb{R}^3$ be the *basal surface* that represents the mountain terrain, the governing equations defined for all points $\mathbf{x}_b \in \mathcal{S}_b$ can be written in Cartesian coordinates as follows:

SPDE-based Savage-Hutter model

$$\frac{\partial h}{\partial t} + \nabla \cdot (h\bar{\mathbf{u}}) = \frac{q_{\mathrm{er}}}{\bar{\rho}_s} \tag{1}$$

$$\frac{\partial(h\bar{\mathbf{u}})}{\partial t} + \mathbf{P}_{\mathbf{n}_b}^{\parallel} \nabla \cdot (h\,\bar{\mathbf{u}} \otimes \bar{\mathbf{u}}) = -\frac{\boldsymbol{\tau}_b}{\bar{\rho}_s} + h\,\mathbf{P}_{\mathbf{n}_b}^{\parallel} \mathbf{g} - \frac{1}{2\bar{\rho}_s} \mathbf{P}_{\mathbf{n}_b}^{\parallel} \nabla(h\,\bar{p}) \tag{2}$$

$$\mathbf{P}_{\mathbf{n}_b}^{\perp} \nabla \cdot (h\,\bar{\mathbf{u}} \otimes \bar{\mathbf{u}}) = h\,\mathbf{P}_{\mathbf{n}_b}^{\perp} \mathbf{g} - \frac{1}{2\bar{\rho}_s} \mathbf{P}_{\mathbf{n}_b}^{\perp} \nabla(h\,\bar{p}) - \frac{\bar{p}}{\bar{\rho}_s} \mathbf{n}_b \tag{3}$$

The unknown fields at $\mathcal{S}_b$ are the avalanche height $h \in \mathbb{R}$, the depth-averaged flow velocity $\bar{\mathbf{u}} = (\bar{u}, \bar{v}, \bar{w}) \in \mathbb{R}^3$, and the basal pressure $\bar{p} \in \mathbb{R}$.

Equation (1) refers to continuity equation, Equations (2) and (3) are the surface-tangential and surface-normal counterparts of the momentum equation, respectively. The normal projection matrix $\mathbf{P}_{\mathbf{n}_b}^{\perp}$ and the tangential projection matrix $\mathbf{P}_{\mathbf{n}_b}^{\parallel}$ are given by:

$$\mathbf{P}_{\mathbf{n}_b}^{\perp} = \mathbf{n}_b \otimes \mathbf{n}_b \quad \text{and} \quad \mathbf{P}_{\mathbf{n}_b}^{\parallel} = \mathbf{I}_3 - \mathbf{P}_{\mathbf{n}_b}^{\perp},$$

where $\mathbf{n}_b \in \mathbb{R}^3$ is the surface normal vector at $\mathbf{x}_b$, $\mathbf{I}_3$ is the identity matrix of order 3, and $\otimes$ denotes the outer product. The basal shear stress $\boldsymbol{\tau}_b$ follows the *Voellmy friction model* [15], [16].

B. Powder-Snow Layer Model

We model the PSL as a two-phase mixture of miscible fluids formed by ambient air and powder-snow in suspension (a snow aerosol). The mixture model represents the multiphase flow as a single-phase fluid, i.e., the two fluid phases are assumed to move at the same average velocity achieved by solving a single momentum equation. In mixture flows, a standard approach is to utilize *volume fractions* [2], [17].
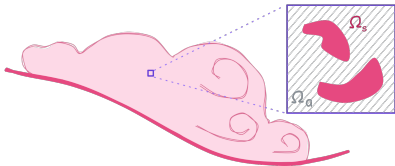

Fig. 3: The powder-snow phase Ω_s and ambient air phase Ω_a can occupy the same volume control Ω in the PSL.

Let $\Omega \subset \mathbb{R}^3$ be a volume control, $\Omega_s \subset \Omega$ the portion occupied by the powder-snow particles, and $\Omega_a \subset \Omega$ the portion occupied by the air (see Figure 3), such that

$$\mathrm{volume}(\Omega) = \mathrm{volume}(\Omega_s) + \mathrm{volume}(\Omega_a). \tag{4}$$

For all $\mathbf{x} \in \Omega$, the volume fractions $\alpha(\mathbf{x}, t), \alpha_a(\mathbf{x}, t) \in [0, 1]$ of the powder-snow and the air, respectively, are computed as follows:

$$\alpha(\mathbf{x}, t) = \frac{\mathrm{volume}(\Omega_s)}{\mathrm{volume}(\Omega)} \quad \text{and} \quad \alpha_a(\mathbf{x}, t) = \frac{\mathrm{volume}(\Omega_a)}{\mathrm{volume}(\Omega)}.$$

Thus, from Equation (4), we have $\alpha_a(\mathbf{x}, t) = 1 - \alpha(\mathbf{x}, t)$. The following convex combination defines the density and the viscosity of the air-snow mixture:

$$\rho = \alpha\,\hat{\rho}_s + (1 - \alpha)\hat{\rho}_a \quad \text{and} \quad \mu = \alpha\,\hat{\mu}_s + (1 - \alpha)\hat{\mu}_a. \tag{5}$$

For simplicity, we assume that the resulting air-snow mixture is an incompressible Newtonian fluid. Therefore, the governing equation for the mixture flow can be expressed as

Mixture flow model

$$\nabla \cdot \hat{\mathbf{u}} = 0 \tag{6}$$

$$\frac{\partial(\rho\hat{\mathbf{u}})}{\partial t} + \nabla \cdot (\rho\,\hat{\mathbf{u}} \otimes \hat{\mathbf{u}}) = -\nabla\hat{p} + \mu\Delta\hat{\mathbf{u}} - (\mathbf{g} \cdot \mathbf{x})\nabla\rho \tag{7}$$

$$\frac{\partial\alpha}{\partial t} + \nabla \cdot (\alpha\,\hat{\mathbf{u}}) = \Gamma\Delta\alpha \tag{8}$$

Equations (6) and (7) are the incompressible Navier-Stokes in conservative form. The dynamic pressure $\hat{p}$ comes from the rewriting of the total mixture pressure p [18]: $p = \hat{p} + \rho\mathbf{g} \cdot \mathbf{x}$. The conservation of the volume fraction α gives rise to an additional convection-diffusion equation (8). The right-hand side of Equation (8) models the diffusive behavior within the mixture, i.e., the dilution of the snow dust by the air. This model relies on *Fick's law* [19] and is used to predict how the concentration (volume fraction) of each mixture constituent varies over time, moving from a region of high concentration to a low concentration across a concentration gradient. The diffusion coefficient Γ encompasses the eddy dispersion and the molecular diffusivity, which describes the diffusion velocity of molecules from the snow phase into the air phase.

C. Transition Layer Model

The TL manages mass addition in PSL from the snow entrainment processes in the interface between the DSL and the PSL. This section presents a novel procedural TL model that considers the snow entrainment as the PSL's primary source of mass and momentum injections. Since the PSL equations describe the powder-snow mass in terms of its concentration $\alpha \in [0, 1]$, the TL model must define an injected mass $\alpha_{\mathrm{inj}} \in [0, 1]$ driven by an vertical injection velocity $\mathbf{u}_{\mathrm{inj}}$.

Injected snow mass

$$\alpha_{\mathrm{inj}} = \omega_\alpha \frac{m_s}{m_V} \quad \text{with} \quad m_V = \hat{\rho}_s V. \tag{9}$$

The value m_V is the maximum snow mass capacity supported by the PSL volume control Ω. The scalar field $\omega_\alpha \in [0, 1]$ is a random density distribution representing snow cover heterogeneity.

Injection velocity

$$\mathbf{u}_{\mathrm{inj}} = -\left(2\frac{q_{\mathrm{er}}}{\bar{\rho}_s} + \omega_{\mathbf{u}}\|\bar{\mathbf{u}}\|_2\right)\mathbf{n}_b. \tag{10}$$

The scalar field $\omega_{\mathbf{u}} \in [0, 1]$ represents a random perturbation that mimics the air entrainment process and turbulent motion in the intermittency region [20].

IV. METHODOLOGY

Our approach consists of three main steps that perform the numerical simulation of each avalanche layer based on FVM. The input values of thickness h_s, provided by the user, give the initial snow cover distribution in the ground layer. The simulations run over discrete meshes representing the terrain surface and the entire computational domain. Following, we will present the FVM discretization of each pipeline step (see Figure 4):
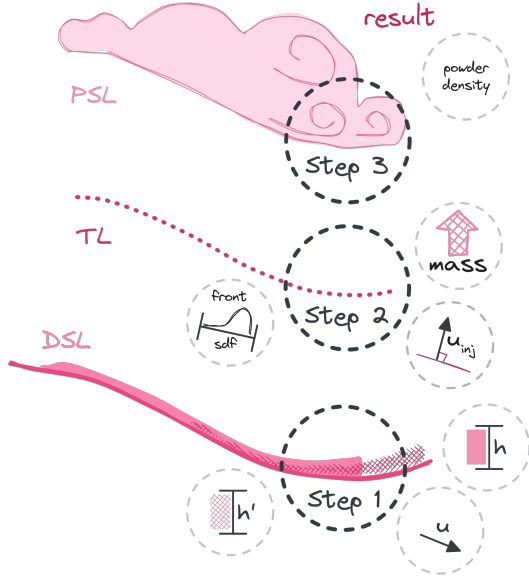

Fig. 4: Overview of the pipeline of our approach.

Step 1. Since it is a one-way coupling system, the simulation of the DSL flow can be executed without any dependency. The two essential resulting quantities are the height h and the DSL velocity $\bar{\mathbf{u}}$;

Step 2. The TL converts the resulting data from the DSL into boundary conditions for the PSL flow. The output is the amount of injected snow mass into the powder cloud and its injection velocity $\mathbf{u}_{\text{inj}}$;

Step 3. The final step simulates the snow cloud of the PSL. The resulting data is a volume fraction field α representing the powder-snow concentration in the computational domain.

A. TL discretization

The TL is implemented as inlet boundary conditions in the PSL. We impose Dirichlet boundary conditions for velocity and snow mass at the terrain mesh. The dynamical boundary values for the powder-snow concentration α_b and the PSL velocity field $\hat{\mathbf{u}}_b$ are defined for each terrain patch face f_b and updated on each time step.
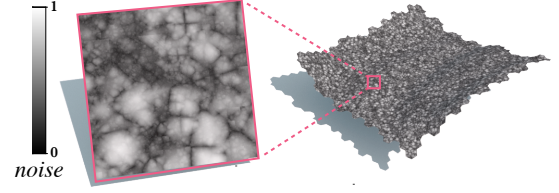

Fig. 5: Procedural noise functions can represent a complex snow cover distribution on a terrain surface. Such random variations in the injection velocity mimic the turbulent behavior of the PSA.

a) Avalanche trigger.: In an avalanche, the suspension of snow particles occurs after the DSL achieves enough velocity and intensifies as the velocity increases [21]. We model this intensity by a sigmoid-like function of the velocity

$$W_{\text{trigger}} = \frac{1}{1 + \exp\left(-\|\bar{\mathbf{u}}\|_2 + U_{\text{min}}\right)},$$

where the value U_{min} controls the minimum velocity required for the powder cloud formation. In our experiments, we use $U_{\text{min}} = 10\,m/s$.

b) Avalanche front.: The eruption entrainment processes intensify in regions closer to the avalanche front [8]. Therefore, the injected mass α_{inj} and the injection velocity $\mathbf{u}_{\text{inj}}$ estimated at terrain position $\mathbf{x}_b$ depend on its distance to the avalanche front $\mathcal{A}_{\text{front}}$. We emulate such dependence by a Gaussian weight function:

$$W_{\text{front}} = \exp\left(-\left[\frac{\text{dist}(\mathbf{x}_b, \mathcal{A}_{\text{front}})}{L_{\text{front}}}\right]^2\right). \quad (11)$$

The value L_{front} represents the *avalanche front size*, i.e., the first L_{front} meters from the leading edge of the avalanche. As the front advances, the distance field $\text{dist}(\mathbf{x}_b, \mathcal{A}_{\text{front}})$ is computed in every time-step by a *front-propagation algorithm* (see Section V-A).

c) Dynamic boundary conditions.: The TL boundary conditions are defined from Equations (9) and (10) and should include the trigger and frontal dynamics of the avalanche.

TL boundary conditions

$$\alpha_b = \gamma_\alpha W \alpha_{\text{inj}} \quad \text{and} \quad \hat{\mathbf{u}}_b = \gamma_{\mathbf{u}} W \mathbf{u}_{\text{inj}} + \bar{\mathbf{u}}, \quad (12)$$

where $W = W_{\text{trigger}} W_{\text{front}}$, the parameters $\gamma_\alpha \in [0, 1]$ and $\gamma_{\mathbf{u}} \in \mathbb{R}^+$ are scaling factors for mass and velocity injection, respectively.

d) Noise function.: A practical solution to model the fields ω_α and $\omega_{\mathbf{u}}$ in Equations (9) and (10), respectively, is to use a procedural noise function that causes random perturbations in the injected snow mass and its injection velocity. In particular we use the *Worley noise* [22], which produces distinct regions resembling natural-like patterns. Figure 5 shows the noise computed over the terrain.

V. GEOMETRIC ALGORITHMS

In the following, we provide details for the geometric algorithms used in our framework.

A. Avalanche Front Distance

The TL depends on the distance from the avalanche front. More specifically, the surface distance $\text{dist}(\mathbf{x}_b, \mathcal{A}_{\text{front}})$ used in Equation (11) approximates the shortest geodesic distance between a point $\mathbf{x}_b$ on the terrain and the front $\mathcal{A}_{\text{front}}$. In fact, the discrete distance field is computed in each cell Ω_K of the DSL mesh $\overline{\mathcal{M}}$, i.e., $dist_K = \text{dist}(\mathbf{c}_K, \mathcal{A}_{\text{front}})$. First, our algorithm detects the cells of $\overline{\mathcal{M}}$ that contain the avalanche front. These *front cells* provide an approximation of $\mathcal{A}_{\text{front}}$. Then, we propagate the discrete distance field $dist$ from the avalanche front to the DSL cells.

a) Front cell detection: The DSL's height h and velocity $\bar{\mathbf{u}}$ specify the front cells. A cell Ω_K is *empty* if its DSL height holds $h_K = 0$. A neighbor cell Ω_N of Ω_K is a *directional neighbor* with direction $\mathbf{d}$ if the ray cast from the centroid $\mathbf{c}_K$ with direction $\mathbf{d}$ intersects the shared edge. Therefore, a cell Ω_K is a front cell if its directional neighbor with direction $\bar{\mathbf{u}}_K$ is empty.

b) Distance propagation: The distance field is propagated from the front cells. The propagation follows the direction against the DSL flow. Given a cell Ω_K, only its non-empty directional neighbors Ω_N in the direction $-\bar{\mathbf{u}}_K$ are considered.

B. Mesh Data Conversion

The PSL cloud can be represented as a volumetric density field, meaning we can render the final result as a volume of a scalar field $F : \mathbb{R}^3 \rightarrow \mathbb{R}$. To convert the mesh data into the scalar volume field, we use a higher-order meshless approximation provided by the *Hermite Radial Basis Function* (HRBF) interpolation [23] combined with *partition of unity* (PU) [23]. Then, we evaluate the HRBF-PU approximation in the centroids of the voxels to achieve the discrete density field for the PSL cloud. In our implementation, the voxels are stored using the sparse grid data structure provided by Open-VDB [24]. Figure 6 compares our HRBF-PU against other meshless methods to demonstrate the interpolation accuracy.

VI. RESULTS

We implemented our framework in C++ using the FVM software package OpenFOAM [25]. Regarding time integration, we use adaptive time-steps managed by the CFL condition. All experiments were performed on a computer equipped with a processor Intel i9-13900k with 24 cores of 3.0GHz and 64GB RAM. The simulations ran in parallel on CPU (up to 20 threads).

Table IV shows the computational times and some statistics for a set of experiments presented in the paper. The first column **simulation** contains the performed experiment (*scene*) using our approach, the dimension (*dim*) of the domain, and the duration (*dur.*) of the resulting animation in seconds. The column **#cells** provides the number of cells of the DSL and
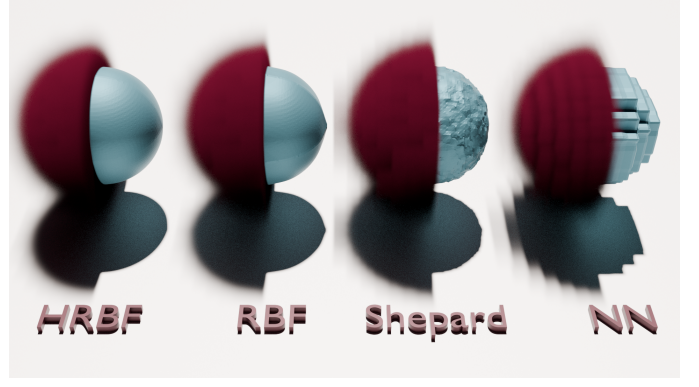

Fig. 6: Interpolating a sampled Gaussian from a coarse to fine grid using our HRBF-PU, RBF-PU, Shepard, and nearest neighbor (NN) interpolation (*from left to right*). As can be seen, the volumetric field (blue) and its isosurface (red) provided by HRBF-PU is more resilient to the aliasing effect.

TABLE III: Model parameters values.

| layer	parameter	description	value
all	g	standard gravity $[m/s^2]$	9.81
DSL	$\bar{\rho}_s$	snow density $[kg/m^3]$	500
	υ	Voellmy's dry friction	0.155
	ξ	Voellmy's dynamic friction $[m/s^2]$	5000
	E_b	specific erosion energy $[m^2/s^2]$	50
TL	γ_α	mass injection factor	0.1
	$\gamma_{\mathbf{u}}$	velocity injection factor	1.6
	L_{front}	avalanche front size $[m]$	80
PSL	$\hat{\rho}_s$	powder-snow density $[kg/m^3]$	1.4
	$\hat{\rho}_a$	air density $[kg/m^3]$	1.2
	$\hat{\mu}_s$	powder-snow viscosity $[m^2/s]$	10^{-4}
	$\hat{\mu}_a$	air viscosity $[m^2/s]$	1.4×10^{-5}
	Γ	diffusion coefficient $[m^2/s]$	2.0×10^4
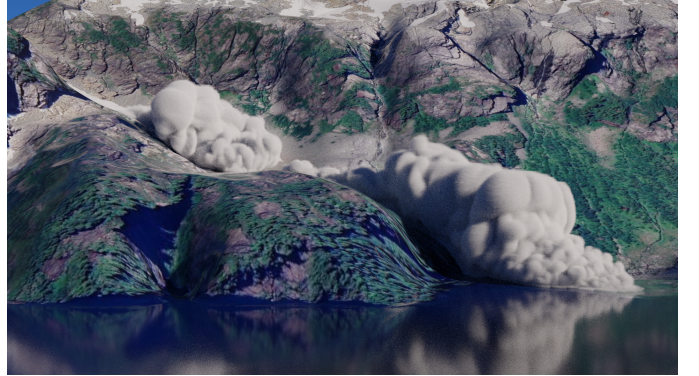
Fig. 7: A powder-snow avalanche simulation at Mount Niobe (Tantalus Range, Canada) using a PSL mesh with 11.4M cells occupying a total volume of $0.17\,km^3$.

PSL meshes. The column $\overline{\delta x}$ presents the average cell sizes in meters. The last column **time** presents the computational times for DSL and PSL (with TL) times in the entire simulation and the average time dt for a single time-step. As can be seen, in 3D simulations, the DSL computational time is less than 1% of the overall simulation time.

TABLE IV: Timings (in seconds), statistics and parameters of our method.

simulation			#cells		$\overline{\delta x}$		time			
scene	*dim*	*dur.*	DSL	PSL	DSL	PSL	*dt*	DSL	PSL	*total*
Fig. 1	3	42	31K	17.8M	7.75	2.99	237.17	74	588224	588298
Fig. 7	3	100	99K	11.4M	37.97	2.47	27.23	535	113568	114103

Procedural and natural mountains: The inherent complexity of procedural and natural terrains shapes the path taken by an avalanche. Figure 1 shows the ability of our method to simulate large-scale PSAs in a synthetic mountain from a height map generated with procedural noise. In addition, we have real-world topographical data, usually represented by a Digital Elevation Model (DEM). Figure 7 shows a PSA simulation at Mount Niobe (Tantalus Range, Canada) from a DEM file provided by [26].

In our related publication [27], we include detailed results exploring important aspects of the flow dynamics and behavior of the avalanche. Some of the covered topics are:

Terrain topography: The geometry of the terrain shapes the path taken by an avalanche. The DSL follows the topography of the terrain, tunneling into fissures, bifurcating over sharp protuberances, and spreading over open areas. The DSL flow's behavior over the terrain's complexities directly impacts the appearance of the PSL cloud.

Slope influence: PSAs may achieve different velocities, heights, and volume profiles of powder clouds due to the influence of the slope. The different velocities result directly from the action of gravity. The greater the angle, the bigger the tangential acceleration.

Ablation and mesh independence studies: In the Supplemental Material of [27], we provide studies about the influence of the parameters and interpolation schemes on the simulation, and its convergence under mesh refinements.

VII. DISCUSSION AND LIMITATIONS

In this section, we discuss some characteristics of our method, highlighting its limitations and potential improvements to the current state of the framework. All experiments and a discussion in depth can be found in [27].

Validation: Ground-truth data for PSAs is scarce in Geoscience, as few studies provide direct measurements. Instead, most rely on photogrammetric analysis to derive key avalanche characteristics, such as plume height and powder cloud volume profiles [10]. In [27], we show that our framework successfully reproduces the height profiles (including the blow-out heights) and the parabolic shape of the PSL volume profiles that closely align with those reported in [10], which validates our method's ability to capture the PSA dynamics.

One-way coupling: Our framework transfers only the snow concentration and momentum from the DSL to PSL, i.e., the PSL simulation does not affect the DSL simulation. Beyond the computational efficiency, the advantage of one-way coupling simulation is that the PSL simulation is agnostic of the method utilized for simulating the DSL.

However, the cells of the DSL mesh and the PSL terrain patch may not share the same geometry or connectivity. Furthermore, since the DSL simulation is independent of the PSL simulation, it may use a different value for the time steps. In order to synchronize the simulations, we interpolate the DSL quantities temporally and spatially between cell centers at the same PSL time level.

Limitations: The current DSL method is limited to mildly curved terrains due to the nature of SWE. Such a model requires small flow heights compared to the curvature. Besides, our method does not deal with discontinuous terrains (e.g., avalanche over a cliff). However, other hybrid alternatives exist, such as the recent use of the MPM method for dense snow flows [9]. We believe this class of particle-mesh methods can bring solutions for both the DSL and the PSL simulations.

VIII. CONCLUSION

We have introduced a computational framework for simulating powder-snow avalanches under complex terrains. Our physically-based approach relies on a multi-layer model that splits the avalanche into two main layers: dense and powder-snow. The dense-snow layer flow is simulated by solving the Savage-Hutter equations, while the powder-snow layer flow is modeled as a miscible air-snow mixture and simulated using the incompressible Navier-Stokes equations. We also present a novel procedural TL modeled as boundary conditions for the snow mass and momentum exchange between the simulation layers. Moreover, we attest with set experiments that our approach provides visually realistic simulations of the turbulent snow cloud rising from an avalanche sliding down a basal surface.

PUBLICATIONS

This text is a short version of the paper [27], which resulted from the related thesis and was presented at SIGGRAPH 2025.

References

[1] C. Ancey, *Geomorphological Fluid Mechanics*. Springer, 2001, ch. Snow Avalanches, pp. 319–338.

[2] D. Dutykh, C. Acary-Robert, and D. Bresch, "Mathematical modeling of powder-snow avalanche flows," *Stud. Appl. Math.*, vol. 127, no. 1, pp. 38–66, 2011.

[3] J. E. Simpson, *Gravity Currents: In the environment and the laboratory*. Cambridge University Press, 1999.

[4] P. Goswami, "Snow and ice animation methods in computer graphics," *Computer Graphics Forum*, vol. 43, no. 2, p. e15059, 2024. [Online]. Available: https://onlinelibrary.wiley.com/doi/abs/10.1111/cgf.15059

[5] B. Turnbull and P. Bartelt, "Mass and momentum balance model of a mixed flowing/powder snow avalanche," *Surv. Geophys.*, vol. 24, no. 5/6, pp. 465–477, 2003.

[6] B. Sovilla, J. N. McElwaine, and M. Y. Louge, "The structure of powder snow avalanches," *C. R. Phys.*, vol. 16, no. 1, pp. 97–104, 2015.

[7] D. Issler, "Dynamically consistent entrainment laws for depth-averaged avalanche models," *J. Fluid Mech.*, vol. 759, pp. 701–738, 2014.

[8] B. Sovilla, P. Burlando, and P. Bartelt, "Field experiments and numerical modeling of mass entrainment in snow avalanches," *J. Geophys. Res. Earth Surf.*, vol. 111, no. F3, 2006. [Online]. Available: https://doi.org/10.1029/2005jf000391

[9] X. Li, B. Sovilla, C. Ligneau, C. Jiang, and J. Gaume, "Different erosion and entrainment mechanisms in snow avalanches," *Mech. Res. Commun.*, vol. 124, p. 103914, 2022.

[10] P. Bartelt, Y. Bühler, O. Buser, and C. Ginzler, "Plume formation in powder snow avalanches," in *International Snow Science Workshop*, 2013.

[11] B. Sovilla, J. N. McElwaine, and A. Köhler, "The intermittency regions of powder snow avalanches," *J. Geophys. Res. Earth Surf.*, vol. 123, no. 10, pp. 2525–2545, 2018.

[12] S. B. Savage and K. Hutter, "The dynamics of avalanches of granular materials from initiation to runout. part i: Analysis," *Acta Mech.*, vol. 86, no. 1-4, pp. 201–223, 1991. [Online]. Available: https://doi.org/10.1007/bf01175958

[13] M. Rauter, A. Kofler, A. Huber, and W. Fellin, "fasavagehutterfoam 1.0: depth-integrated simulation of dense snow avalanches on natural terrain with openfoam," *Geosci. Model Dev.*, vol. 11, no. 7, pp. 2923–2939, 2018.

[14] M. Rauter and Z. Tukovic, "A finite area scheme for shallow granular flows on three-dimensional surfaces," *Comput. Fluids*, vol. 166, pp. 184–199, 2018.

[15] A. Voellmy, "Über die zerstörungskraft von lawinen," vol. 73, pp. 212–217, 1955.

[16] M. Christen, J. Kowalski, and P. Bartelt, "Ramms: Numerical simulation of dense snow avalanches in three-dimensional terrain," *Cold Reg. Sci. Technol.*, vol. 63, no. 1-2, pp. 1–14, 2010.

[17] Y. Xu, X. Wang, J. Wang, C. Song, T. Wang, Y. Zhang, J. Chang, J. J. Zhang, J. Kosinka, A. Telea, and X. Ban, "An implicitly stable mixture model for dynamic multi-fluid simulations," in *SIGGRAPH Asia 2023*, 2023.

[18] H. Rusche, "Computational fluid dynamics of dispersed two-phase flows at high phase fractions," PhD Thesis, Imperial College London, 2002. [Online]. Available: http://hdl.handle.net/10044/1/8110

[19] J. Etienne, P. Saramito, and E. J. Hopfinger, "Numerical simulations of dense clouds on steep slopes: application to powder-snow avalanches," *Ann. Glaciol.*, vol. 38, pp. 379–383, 2004.

[20] K. Ivanova, A. Caviezel, Y. Bühler, and P. Bartelt, "Numerical modelling of turbulent geophysical flows using a hyperbolic shear shallow water model: Application to powder snow avalanches," *Comput. Fluids*, vol. 233, p. 105211, 2022.

[21] P. Bartelt, O. Buser, C. Vera Valero, and Y. Bühler, "Configurational energy and the formation of mixed flowing/powder snow and ice avalanches," *Ann. Glaciol.*, vol. 57, no. 71, pp. 179–188, 2016.

[22] S. Worley, "A cellular texture basis function," in *SIGGRAPH '96*, 1996.

[23] G. F. Fasshauer, *Meshfree Approximation Methods with MATLAB*. World Scientific Publishing, 2007.

[24] K. Museth, "Vdb: High-resolution sparse volumes with dynamic topology," *ACM Trans. Graph.*, vol. 32, no. 3, pp. 1–22, 2013.

[25] C. Greenshields, *OpenFOAM v12 User Guide*. The OpenFOAM Foundation, 2024. [Online]. Available: https://doc.cfd.direct/openfoam/user-guide-v12

[26] U.S. Geological Survey, "1/3rd arc-second digital elevation models (dems) - usgs national map 3dep downloadable data collection," 2024. [Online]. Available: https://www.usgs.gov

[27] F. Nascimento, F. S. Sousa, and A. Paiva, "Digital animation of powder-snow avalanches," *ACM Trans. Graph.*, vol. 44, no. 4, 2025.